16th World Conference on Earthquake, 16WCEE 2017
Santiago Chile, January 9th to 13th 2017
Paper N° 1496
Registration Code: S-A1464528184

NUMERICAL STUDY ABOUT EFFECT OF DISTRIBUTION OF THICKNESS AND STRENGTH OF LIQUEFIABLE LAYER ON GROUND DEFORMATION

T. Matsumaru[(1)], T. Sato[(2)] and A. Kudo[(3)]

[(1)] *Assistant senior researcher, Railway Technical Research Institute, matsumaru.takaki.35@rtri.or.jp*
[(2)] *Researcher, Railway Technical Research Institute, sato.taketo.67@rtri.or.jp*
[(3)] *Deputy Manager, JR East Consultants Company, a-kudo@jrc.jregroup.ne.jp*

Abstract

When the liquefaction of the ground occurs, the settlement is often caused due to the shear deformation during the earthquake and the consolidation after the earthquake. However, this settlement does not occur regularly but usually varies in the space. One of the reasons of this variety would exist in the liquefiable layer itself, such as the thickness of the layer and the liquefaction resistance. However, it is not easy to identify the reasons and to predict such an irregular settlement in the field.

In this paper, a series of effective stress analyses were performed in order to clarify these effects on irregular settlement.

A railway yard damaged in the 2011 off the Pacific coast of Tohoku earthquake was selected as the objective for conducting numerical simulations. In this field, the coal ash under the railway track would have been liquefied. The layer under the coal ash was alluvial clay layer of about 20 m in thickness with a small N-value of SPT. The coal ash produced by steam locomotives was presumably deposited in the field in order to keep the height of the railway tracks against the consolidation of the clay layer. The height of the railway tracks after the earthquake was measured and the surface layer survey was conducted precisely in order to clarify the structure of the liquefiable layer. From these surveys, the settlement of the railway tracks has good correlation with the distributions of the thickness of the liquefiable layer and the liquefaction strength.

In the simulations, five cases of calculations were performed. In Cases 1 and 2, 1-dimensional dynamic response analyses were conducted in which the horizontally layered ground was supposed. The maximum and minimum thicknesses of the liquefiable layer were supposed in Cases 1 and 2 based on the survey. In Case 3, 2-dimensional model in consideration of the distributions of the thickness of the layers at the field was prepared. In Cases 4 and 5, the distributions of the liquefaction strength were considered in the same model as in Case 3.

Among the series of simulations, the simulation in Case 3 in consideration of the distributions of the thickness of the liquefiable layer reproduced well the measured settlement. On the other hand, 1-dimensional analysis showed smaller settlement even if the maximum thickness of the liquefiable layer was considered. Though the tendencies for the excess pore water pressure to increase with increasing thickness of the liquefiable layer in Case 3 were almost the same as those obtained from 1-dimensional analyses in Cases 1 and 2, the time histories of the displacement were different. This would be caused by the increased response of acceleration in the space due to the distributed layer. Furthermore, the settlement due to the consolidation after the earthquake was different from Cases 1 and 2.

The simulations of Cases 4 and 5 in consideration of the distributed liquefaction strength showed better coincidence with the measured settlement than Case 3. In these cases, the occurrence of the liquefaction changed partially according to the strength of liquefaction. Therefore, larger settlement was evaluated in the region where the liquefaction strength decreased.

Keywords: liquefaction, irregular settlement, effective stress analysis

1. Introduction

In the 2011 off the Pacific coast of Tohoku earthquake in Japan, a huge number of sandy grounds were liquefied due to the long duration of the earthquake [1 – 3]. At Sendai airport, countermeasure works against liquefaction had been conducted partially before this earthquake, so the occurrence of liquefaction was able to be successfully prevented to some extent. However, liquefaction occurred at the place without any countermeasure works and the irregular settlement occurred in the space. This kind of irregular settlement is often seen after the earthquake and still be a problematic issue. In order to keep or recover early the traffic services of road, railway and airport, it is important to make the mechanism of the occurrence of the irregular settlement caused by liquefaction clear and prevent that from occurring.

There would be some reasons for this kind of irregular settlement. From the point of view of a liquefiable layer, an irregular distribution of the thickness or the liquefaction resistance may be one of the reasons. Therefore, some shaking table tests of model ground with a focus these factors were conducted [4]. Shaking table tests aimed at setting the optimal arrangement of liquefaction countermeasure works were also conducted to reduce the settlement after the earthquake [5].

Using numerical techniques, Nakai et al. [6] showed that the deformation of the ground was strongly affected by the spatial distribution of the structures of geological layers. However, they focused on the distributions of non-liquefiable layer or its inclination under the liquefiable layer. Miyata et al. [7] proposed a method of predicting the settlement after the occurrence of liquefaction by combining 1-dimensional seismic response analysis and Monte Carlo method. However, they only applied their method to model ground, so the validation of their method is not still confirmed. As shown here, the mechanism of irregular settlement caused by the distributions of the thickness or the strength of a liquefiable layer has not been made clear and the evaluation method should be developed.

In this paper, in order to show the effect of the distributions of the thickness or strength of liquefiable layers on irregular settlement, a series of effective stress analyses were conducted. As an exemplary field for conducting numerical simulations, the railway yard damaged in the 2011 off the Pacific coast of Tohoku earthquake was selected. In this field, the distributions of the thickness and the shear wave velocity were roughly obtained across the railway tracks by using the surface wave method. Furthermore, the relative settlement of the railway tracks after the earthquake were also measured. Therefore, in the numerical studies, it is possible to consider the field conditions and to compare the calculated results with the measurement. In the analyses, the effect of the distributions of the liquefiable layer was evaluated by comparison between the 2-dimensional analysis in consideration of the distributions of the thickness and the 1-dimensional analysis. The effect of the distributions of the liquefaction strength was examined by the calculation by means of 2-dimensional model in consideration of the distribution of liquefaction resistance based on the amount of shear wave velocity.

2. Outline of damage and properties at targeted field

In this study, we selected a railway yard damaged by the occurrence of liquefaction in the 2011 off the Pacific coast of Tohoku earthquake. Severe damage occurred to the railway tracks and structures, so the operation of the railway was stopped. The railway tracks showed irregular deformation in both the horizontal and vertical directions. Fig. 1 shows the typical distributions of the N-value of SPT and shear wave velocity measured by the PS logging at this field [8]. At the surface, the coal ash was deposited under the railway track and liquefaction would occur at this layer. The layer under the coal ash was an alluvial clay layer (Ac1, Ac2 and Ac4) about 20 m in thickness with a small N-value. The water level was located at GL-1.0 m.

In order to make the characteristic of the coal ash clear, physical properties, permeability, and the feature of compaction were evaluated by laboratory tests [9]. Table 1 shows the test results. The value of the soil particle was smaller than usual sand and close to that surveyed by other researchers [10]. The dry density was smaller and the void ratio was larger than usual sand. However, the dry density was almost the same as its maximum dry density obtained by a compaction test in a laboratory. Therefore, the small dry density is caused by the small soil particle gravity. The liquefaction resistance was evaluated by cyclic triaxial tests and the test results will be mentioned in chapter 4.

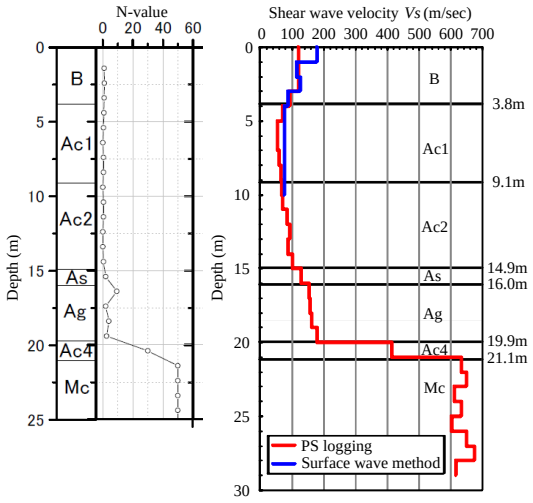

Fig. 1 – Distribution of N-value and shear wave velocity [8]

Table. 1 – Material properties of coal ash [9]

Soil particle density G_s	2.326~2.484
Dry density ρ_d	0.843~0.949 g/cm^3
Void ratio e	1.624~1.774
Fine fraction content F_c	9~19%
50 % diameter D_{50}	1.40~2.30mm
10 % diameter D_{10}	0.0021~0.083mm
Permeabilty coefficient k	1.42 ×10^{-4} m/s
Internal friction angle φ	42.3 degree
Cohesion c	4.7 kPa
Maximum dry density ρ_{dmax}	1.070~1.295 g/cm^3
Optimal water content w_{opt}	28.6~41.4%

At this field, the surface wave method was applied in order to make clear the geological structure, after the earthquake [8]. In Fig. 1, the shear wave velocity obtained by the surface wave method at the same position where the PS logging was conducted was also plotted. The shear wave velocity obtained by the surface wave method agreed well with the velocity measured by the PS logging. Fig. 2 shows the distribution of the shear wave velocity attained from the surface wave method along the railway tracks. In this figure, the line of a shear wave velocity of 100 m/s was emphasized because the bottom of the liquefiable coal ash layer (B) could be estimated from this shear wave velocity, as shown in Fig. 1. It is found that the thickness of the liquefiable layer under the ground water level was distributed in the range from 1.0 m to 2.5 m and the shear wave velocity was also distributed in the range from 100 m/s to 170 m/s.

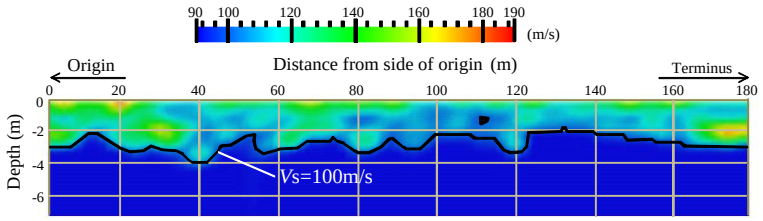

Fig. 2 – Distribution of shear wave velocity by surface wave method [9]

3. Analytical method

In this study, the governing equations for three phase mixture (soil particle, pore water, and pore air) were adopted [11]. However, only saturated soils are considered in this analysis, so the phase of pore air is neglected. The governing equations were formulated based on the following assumptions:

1) The conditions are isothermal;
2) The soil particles are incompressible;
3) The mass exchange among phases can be neglected;
4) The material time derivative of relative velocities and the advection terms of pore fluids to the soil skeleton can be neglected.

The governing equations consist of the momentum balance equations of mixtures and the mass and momentum balance equations of pore water.

The weak forms were implemented in finite element formulation. The Newmark implicit scheme is used for time integration. The primary variables are the second-order material time derivatives of the displacement of soil skeleton $\mathbf{a}^s$, and pore water pressure $\ddot{p}^w$. The weak forms are linearized and solved by the Newton-Raphson method iteratively at each time step. In the finite element formulation, Galerkin method and isoparametric 8-node elements are used. The soil skeleton displacement and the fluid pressures are approximated at 8 nodes and 4 nodes respectively to satisfy the discrete LBB conditions for the locally undrained case.

For the constitutive equation for liquefiable sand, a cyclic elasto-plastic model [12] was applied. This constitutive model was formulated on the following assumptions:

1) The infinitesimal strain theory;
2) The elasto-plastic theory;
3) The non-associated flow rule and the Cam-clay type plastic potential function [13] ;
4) The non-linear kinematic hardening rule [14] and the dependency of hardening parameters on the amount of plastic strain.

Using the model, we succeeded in reproducing the experimental results well under various stress conditions and the model was applied to simulations treating liquefaction of ground and embankment.

4. Numerical study about distribution of thickness of liquefiable layer

4.1 Outline of analysis

In order to show the effect of the distribution of the thickness of the liquefiable layer on the irregular settlement, a series of the analyses were carried out. Based on the boundary between liquefiable coal ash layer (B) and the clayey layer (Ac1) whose thickness was obtained by the surface wave method, we prepared a 2-dimensional model and conducted its effective stress analysis. For comparison, we conducted 1-dimensional analyses in which the maximum and minimum measured thicknesses of the liquefiable layer were modeled.

4.2 Analytical conditions

Fig. 3 shows the analytical models of the ground. For simplicity, As, Ag and Ac4 were not considered in the models because these layers were not distributed continuously in the region of the analytical model. In Cases 1 and 2, 1-dimensional soil column models were prepared based on the assumption of the horizontal stratification. The thickness of the liquefiable layer was set at 2.5 m in Case 1 and 1.0 m in Case 2, based on the maximum and minimum thicknesses obtained by the surface wave method.

In Case 3, 2-dimensional ground model was prepared considering the distribution of the thickness of the liquefiable layer (B) along the railway tracks. The thickness of the clayey layers (Ac1 and Ac2) would have some distributions of the thickness. However, there is no enough evidence for its distribution and the aim of the analysis is evaluating the effect of the distribution of the thickness of the liquefiable layer on the irregular settlement after the earthquake. So, the distribution of the thickness was taken into account only with regard to the liquefiable layer. In this model, we installed horizontal wide elements, which behave as a free field at both edges of the model in order to decrease the influence of the reflected wave from the edges.

The cyclic elasto-plastic constitutive model was applied to the liquefiable layer. The parameters of the constitutive model for the soil skeleton in Table 2 were determined according to the following steps. The parameters, K^*, G^*, b and M_m were determined by monotonic drained triaxial tests and cyclic undrained triaxial tests. The remaining parameters were determined by adjusting technique in which the values of the parameters were selected to describe the liquefaction strength curve, the effective stress path and stress-strain relation of the undrained cyclic triaxial tests for evaluating the liquefaction resistance in saturated conditions.

For the clayey layers (Ac1 and Ac2), the elaso-plasitc model was also applied. However, The dilatancy parameters D was set to zero because of avoiding the occurence of liquefaction in these two layers. For the Mc layer located at the bottom of the model, the elastic model was used.

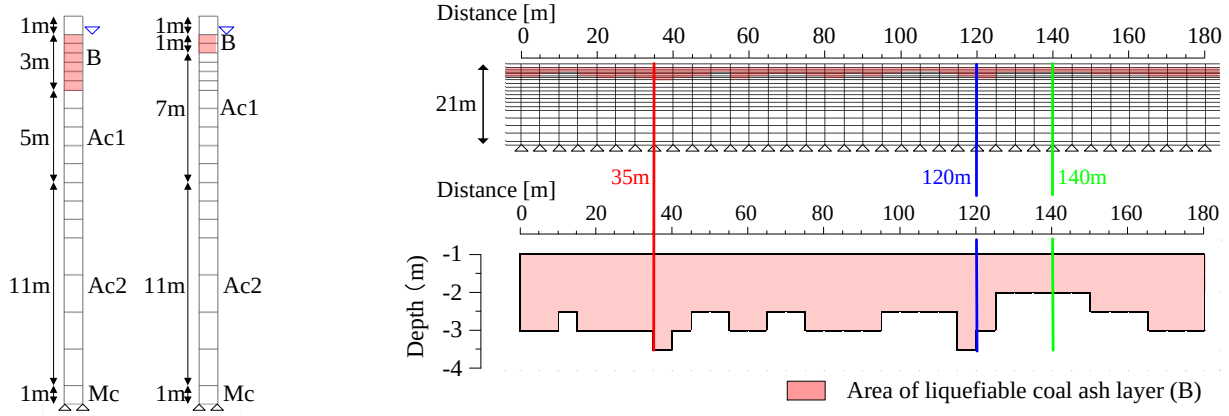

(a) 1-dimensional model (b) 2-dimensional model

Fig. 3 – Analytical model of ground

Table 2 – Material parameters

	B	**Ac1**	**Ac2**	**Mc**
Inital porosity, n_0	0.638	0.783	0.711	0.51
Real density of soil particle, ρ^{sR} (g/cm^3)	2.326	2.541	2.633	2.710
Permeability coefficient k_w^s(m/s)	1.42×10^{-5}	6.39×10^{-9}	6.61×10^{-9}	7.51×10^{-7}
Bulk modulus, K*	1263	586	726	--
Shear modulus, G*	583	126	156	--
Nonlinear hardening parameter, a_0	1200	300	400	--
Nonlinear hardening parameter, a_1	100	20	30	--
Nonlinear hardening parameter, b	-1.73	-1.77	-1.36	--
Nonlinear hardening parameter, C_f	3500	2000	2000	--
Critical state stress ratio, M_m	1.73	1.77	1.36	--
Coefficient of dilatancy, D	0.1	0	0	--
Yield function parameter, k	0.05	0.05	0.05	--
Elastic modulus, λ (kPa)	--	--	--	703033
Elastic modulus, μ(kPa)	--	--	--	247000

Fig. 4 shows the comparison of the stress pass (relationship between mean effective stress and stress difference) and the stress-strain relationship (relationship between axial strain and stress difference), obtained by the cyclic triaxial tests using the coal ash and their simulation. The simulation well reproduced the behavior of the experimental result.

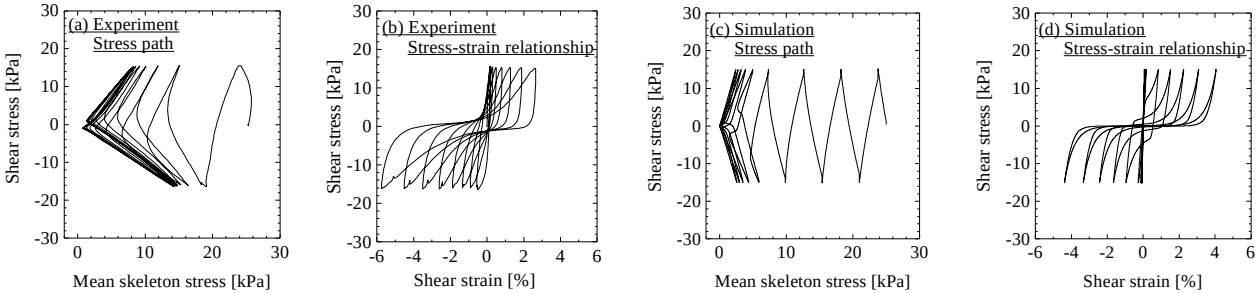

Fig. 4 – Time history of input motion

Fig. 5 shows the time history of the estimated ground motion used in the dynamic response analysis. The procedure for estimating the input motion is as follows. First, the recorded motion at K-NET Mito was transferred to the base motion at the same point by deconvolution using the equivalent linearization method. Then, the base motion at the location of the railway yard was modified by adjusting its amplitude considering the distance from the seismic origin. Finally, the input motion was calculated by one-dimensional seismic response analysis using this modified base motion. The maximum acceleration of the estimated ground motion was 567 gal. This motion was set at the bottom of the finite element model.

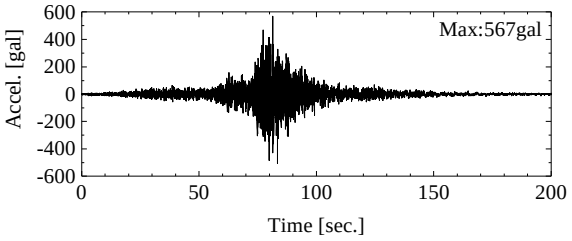

Fig. 5 – Time history of input motion

In the dynamic response analysis, a time integration step of 0.002 second was adopted for 200 seconds. During this period, the earthquake motion shown in Fig. 5 was inputted. After this time, a time integration step was gradually increased and became 10 second at the end of the calculation. The total time considered in the calculation was 10,000 seconds, in order to evaluate not only the dynamic behavior induced by the earthquake but also the settlement due to the consolidation after the earthquake. Hysteresis damping by the constitutive model was basically used, and Rayleigh damping proportional to the initial stiffness was adopted in order to describe the damping especially in the high frequency domain. The factor of Rayleigh damping was set to 0.002.

4.3 Results and discussions

Fig. 6 shows the longitudinal distribution of the amounts of settlement of the ground surface at the end of the simulations. In this figure, the relative height of the railway track measured at the field after the earthquake was also plotted. The measured relative settlement was initialized at 0 at the position of 0 m. As the result of the comparison, it turns out that, as far as the settlement is concerned, the result of the evaluation by the 2-dimensional analysis (Case 3) reproduced the result obtained by the measurement well, because the maximum settlement occurred at the same position as that obtained from the measurement and the amount also coincided with the measurement. However, from a position of 150 m to the end, the tendency of the settlement did not coincide with the measurement. The reason of this difference would be caused by the boundary condition as a free field at both the edges though the railway track at the field was fixed by a concrete block for a train stop.

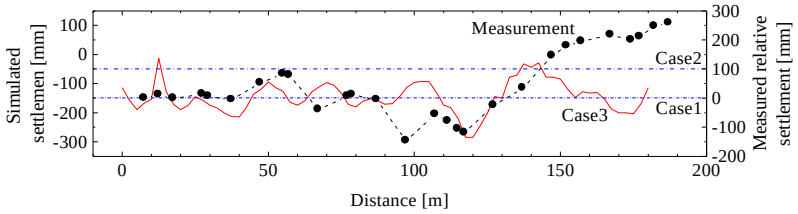

Fig. 6 – Distribution of settlement obtained by simulations and measured relative height of ground surface

Then, we will focus on the difference of the simulated settlement between 1-dimensional analyses (Cases 1 and 2) and 2-dimensional analysis (Case 3). In the model of Case 3, the height of the liquefiable layer is about 2.5m at positions from 20 m to 50 m, and about 1.0 m at positions from 130 m to 150 m, which coincide with the height of the liquefiable layer of Cases 1 and 2. Due to the coincidence of the height of the liquefiable layer, the settlements simulated in Cases 1 and 2 would almost coincide with the settlement at these positions in Case 3. However, the maximum settlement occurred at a position of 120 m in Case 3 exceeded the settlement calculated in Case 1 largely. This would be caused by the special distribution of the liquefiable layer in Case 3.

In Case 3, we pick up the nodal and elemental behaviors at positions of 35 m and 120 m, where the height of the liquefiable layer is 2.5 m, and at a position of 140 m, where the height is 1.0 m, in order to focus on the differences of the behaviors among the three cases. Fig. 7 shows the time histories of the vertical displacement at the surface of the ground located at these positions. The time histories were separated into (a) and (b), during and after the earthquake. In the time histories of (a), the vertical displacement in three cases, and that at three points in Case 3 started to differ at about 30 seconds (denoting about 30 seconds after the beginning, the same as follows). Particularly, the vertical displacement at a position of 140 m in Case 3 shows uplift during a period from 30 to 100 seconds, which was observed neither in Case 1 or 2. At the end of the earthquake, the maximum difference of the displacement at the three nodes in Case 3 was about 10 cm, and the difference between the nodal points at 35 m and at 120 m was about 5 cm. After the earthquake, these differences became larger due to the settlement by consolidation, as shown in Fig. 7 (b).

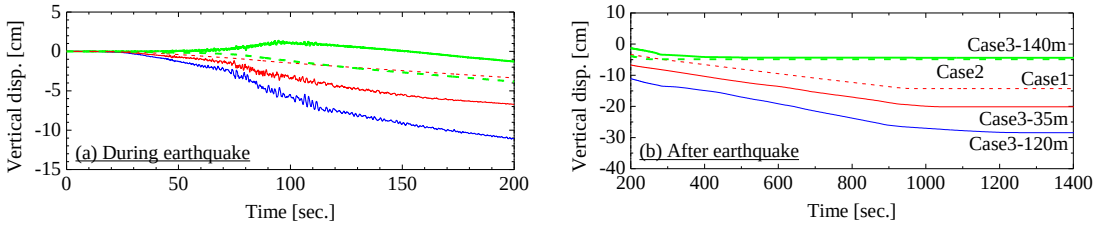

Fig. 7 – Time histories of vertical displacement at surface of ground

Fig. 8 shows the time histories of the excess pore water pressure ratio (E.P.W.P.R.) at depths of GL-1.75 m and GL-2.75 m during the earthquake. Liquefaction occurred at about 50 seconds in Case 1 and at about 80 seconds in Case 2. In Case 3, liquefaction occurred at 50 second at the positions of 35 m and 120 m, and at 80 second at 120 m. This means that the time of the occurrence of liquefaction would only depend on the thickness of the liquefiable layer. Particularly, the difference in the time of the occurrence of the liquefaction between the nodes located at positions of 120 m and 140 m was about 30 seconds even though the distance between these two nodal points was only 20 m.

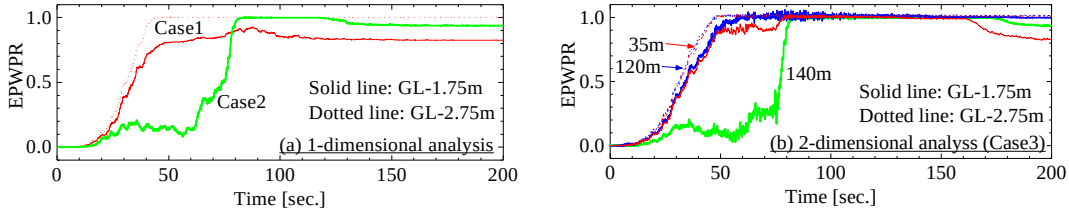

Fig. 8 – Time histories of E.P.W.P.R.

Fig. 9 shows the time histories of acceleration at each nodal point. With a focus on the response obtained in the 1-dimensional analyses, the response in Case 1 became smaller after 50 seconds, compared to that in Case 2. In Case 1, the thickness of the liquefiable layer was larger and the occurrence of liquefaction was earlier as shown in Fig. 8 (a). This would cause the larger reduction of the response of acceleration. However, in the result of the simulation of Case 3, the difference in the responses of the acceleration among the three nodal points was smaller than the difference of the 1-dimensional analyses. Particularly, the response at 120 m was larger than that at 35 m and that in Case 1. Around this position, the thickness of the liquefiable layer was largely changed and the time of the occurrence of liquefaction largely differed as shown in Fig. 8 (b). Affected by the dynamic behavior of the surrounding ground, the response of acceleration at a position of 120 m would not decrease largely. This behavior would also cause larger settlement at this position during the earthquake, as shown in Fig. 7 (a).

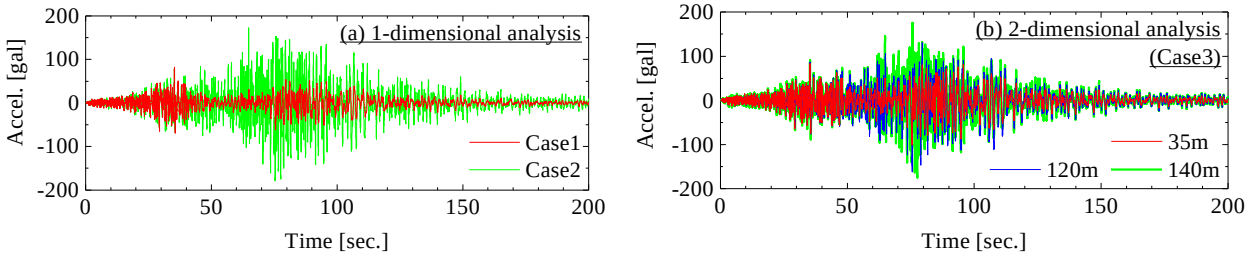

Fig. 9 – Time histories of acceliration

Fig. 10 shows the times history of the excess pore water pressure ratio at a depth of GL-1.75 m after the earthquake. The tendency of the decrease of the excess pore water pressure ratio at positions of 35 m and 140 m in Case 3 was similar to those in Cases 1 and 2. The thickness of the liquefiable layer would also affect the dissipation of excess pore water pressure. The time when the excess pore water pressure was perfectly dissipated almost coincided with the time when the vertical displacement stopped as shown in Fig. 7 (b). The difference between the 1-dimensional and the 2-dimensional analyses was small, from the point of view of the dissipation of the excess pore water pressure. However, it took a little bit longer time for the pore water pressure to dissipate at a position of 120 m in Case 3. This would cause a larger increase in the vertical displacement at this position.

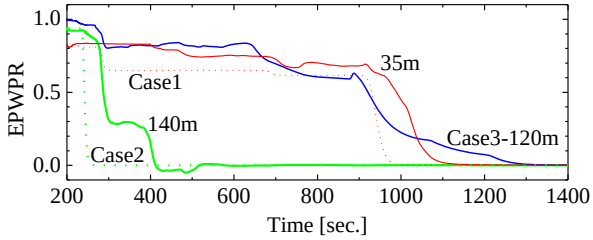

Fig. 10 – Time histories of E.P.W.P.R. after earthquake

5. Numerical study about distribution of strength of liquefiable layer

5.1 Outline of analysis

In this chapter, we focused on the effect of the distribution of the liquefaction strength on the irregular settlement. Based on the result of the shear wave velocity measured by the surface wave method, the distribution of the liquefaction strength in the 2-dimensional model was assumed and effective stress analyses were carried out. The simulated results were compared to the results obtained without considering the distribution.

5.2 Analytical conditions

It is well known that the shear wave velocity and the liquefaction resistance have relationship [15]. The specimens used for the cyclic triaxial tests showed a shear wave velocity of about 120 m/s. However, we did not conduct cyclic triaxial tests using the specimens with different shear wave velocity. Therefore, it was assumed

that the liquefaction resistance of the coal ash ground was categorized into three degree of strength according to the shear wave velocity as shown in Table 3. The middle strength was defined as being based on the liquefaction properties shown in Table 2 and Fig. 4. The small and large strength was modeled using different set of parameters mentioned later. We conducted two analyses of Cases 4 and 5. The shear wave velocity of the boundary value between the small and the middle liquefaction resistance was different between Cases 4 and 5. Fig. 11 shows the distributions of the liquefaction resistance considered in the finite element model in Cases 4 and 5. In Case 4, the area of the small liquefaction resistance is located partially at positions from 80 m to 120 m. However, this area is distributed around a position of 40 m and widely at positions from 80 m to 160 m in Case 5.

Table 3 – Relationship between shear wave velocity and liquefaction resistance

Liquefaction resistance		**Small**	**Middle**	**Large**
Shear wave velocity (m/s)	**Case4**	$V_s < 105$	$105 \leqq V_s < 140$	$140 \leqq V_s$
	Case5	$V_s < 110$	$110 \leqq V_s < 140$	$140 \leqq V_s$

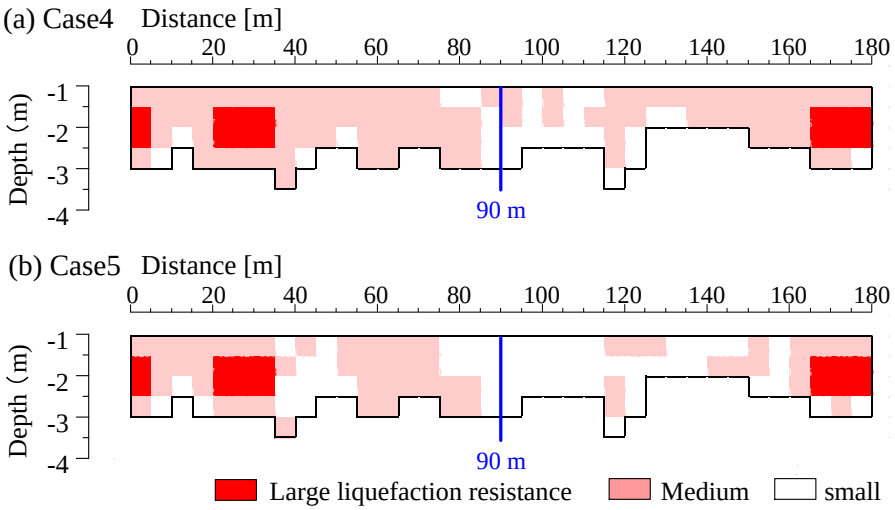

Fig. 11 – Distributions of shear wave velocity in finite element model

It is possible that some physical parameters are changed according to the value of the shear wave velocity. However, for simplicity, the model parameters for describing the small and large liquefaction resistance were controlled only by the two parameters, that is, hardening parameters of a_0 and C_f. Table 4 shows the determined parameters and Fig. 12 shows the stress pass and stress-strain relationship obtained from calculation by use of these parameters. Compared to the behavior obtained by the simulation for the specimen of the middle liquefaction resistance, the simulations for the specimens with the small and large liquefaction resistance could describe the change of the stress pass and the stress-strain relationship.

Table 4 – Detemined parameters for material of small and large liquefaction resistance

Liquefaction Resistance	**Small**	**Large**
Nonlinear hardening parameter, a_0	600	3500
Nonlinear hardening parameter, C_f	1400	12000

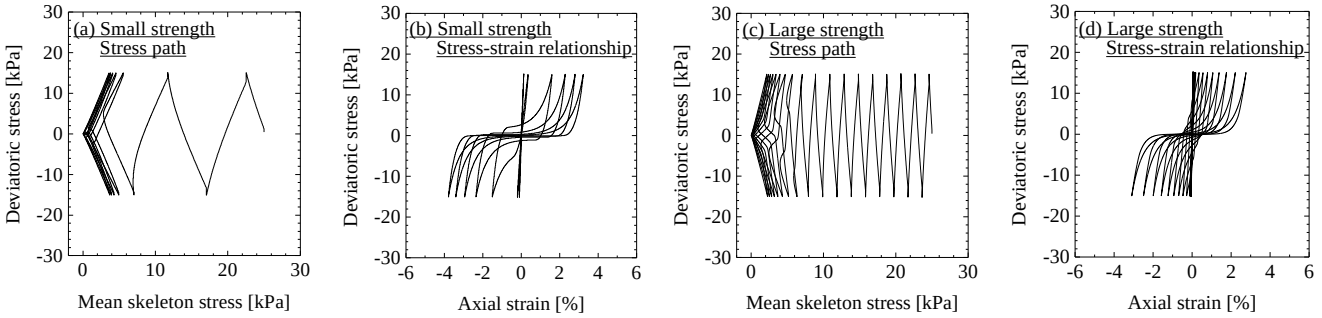

Fig. 12 – Stress pass and stress-strain relationship for small and large liquefaction resistance

5.3 Results and discussions

Fig. 13 shows the longitudinal distributions of the amounts of settlement at the ground surface obtained by the simulations of Cases 4 and 5, including the result obtained by the simulation in Case 3 and the measured of measured relative settlement. Though the reproduction of the large settlement around a position of 100 m was difficult in the simulation in Case 3, the simulations in Cases 4 and 5, where the special distributions of liquefaction were considered, shows improvement in the reproduction of the measured settlement around this position. However, in the simulations, the maximum settlement was obtained at a position of 90 m, so the position did not perfectly coincide with the measurement.

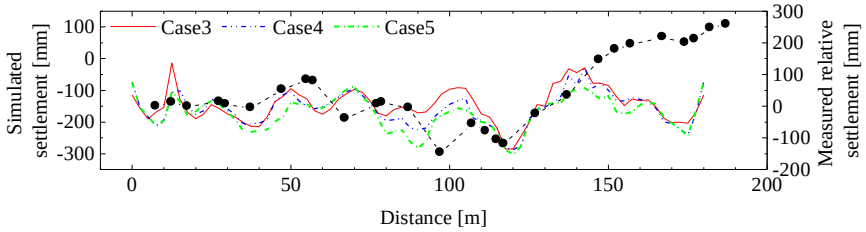

Fig. 13 – Distribution of settlement obtained by simulations and measured relative height of ground surface

In order to clarify the reason of the difference among the three cases, we focused on the behavior of the ground at a position of 90 m. Fig. 14 shows the time histories of the vertical displacement at this position. As shown in Fig. 14 (a), the vertical displacement for these three cases almost coincided during the earthquake. However, after the earthquake, the time when the vertical displacement stopped differed, as shown in Fig. 14 (b). Because the liquefaction around this position was different among three cases, the time would be delayed and the amount of the settlement became larger according to the ratio of the region of the small liquefaction resistance.

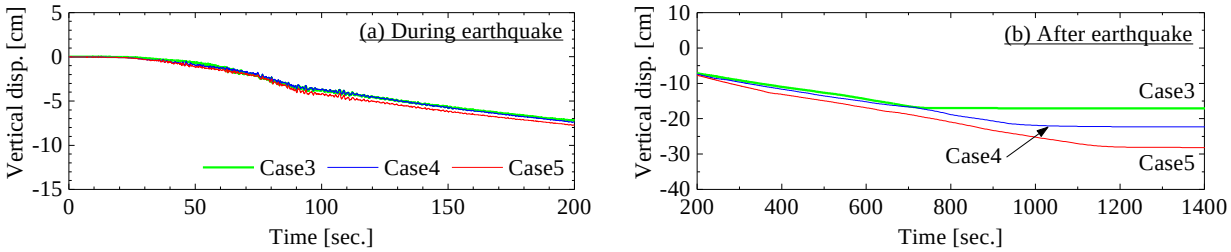

Fig. 14 – Time histories of vertical displacement at surface of ground

Fig. 15 shows the time histories of the excess pore water pressure ratio at a depth of GL-1.75 m. In Cases 4 and 5, liquefaction occurred at about 35 seconds, earlier than in Case 3. In the analytical model of Cases 4 and 5, material with small liquefaction resistance occupied this position, so liquefaction would occur earlier than in Case 3.

Fig. 16 shows the time histories of acceleration at the surface of the ground at a position of 90 m. According to the difference in the behaviors of the excess pore water pressure, the response of the acceleration in

Cases 4 and 5 becomes smaller from 30 to 75 second, compared to that in Case 3. However, the responses in the three cases almost coincided again after 75 second because the ground would have been liquefied perfectly around this position before this time in all cases.

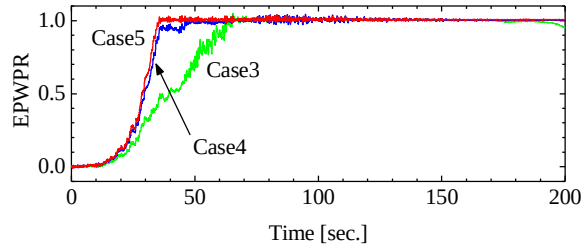

Fig. 15 – Time histories of E.P.W.P.R.

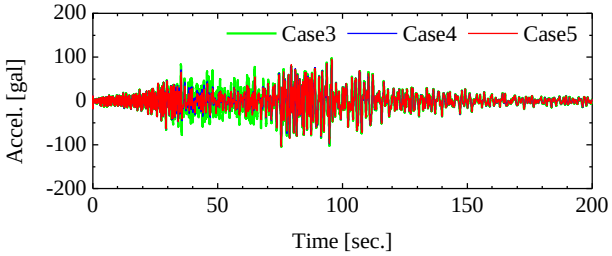

Fig. 16 – Time history of acceleration

Fig. 17 shows the time histories of the excess pore water pressure ratio after the earthquake. For all cases, the excess pore water pressure ratio came back to zero after the earthquake, but the time when the value reached zero was different among the three cases. It seems that the shear strain for the recovery of the stiffness in the liquefied layer was affected by the liquefaction strength. For the layer with small liquefaction resistance, the stiffness would be recovered after larger strain appeared than for the layer with the middle or large liquefaction resistance.

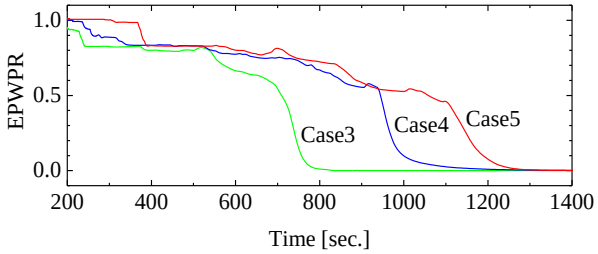

Fig. 17 – Time histories of E.P.W.P.R. after earthquake

6. Conclusions

A series of the effective stress analyses were performed in order to clarify the reasons of the irregular settlement of the ground after the occurrence of liquefaction. As the objective of the analyses, the railway yard damaged in the 2011 off the Pacific coast of Tohoku earthquake was selected. In this field, the surface wave method was applied and it was revealed that the liquefiable layer has the special distributions of thickness and strength. In the series of the simulations, we focused on these effects on the irregular settlements.

First, 2-dimensional analysis in consideration of the distribution of the thickness of the liquefiable layer was performed. The simulation result reproduced the settlement measured at the field to some extent. Compared to the 1-dimensional analysis in which the maximum thickness of the liquefiable layer is assumed, the settlement obtained from the 2-dimensional analysis became larger. The difference in the dimension of the analyses showed that the responses of the acceleration were largely affected by the distribution of the thickness of the liquefiable layer though the process of the increase of the excess pore water pressure would depend on the local thickness.

Furthermore, 2-dimensional analyses in consideration of the distribution of the liquefaction resistance were conducted. By considering the distribution, the degree of the reproduction of the measured settlement was improved. During the earthquake, the time of the occurrence of the liquefaction and the response of the acceleration were affected by the resistance, but the amount of the settlement showed little difference. After the earthquake, the settlement caused by consolidation was changed depending on the distribution of the liquefaction resistance because the dissipation of the excess pore water pressure was influenced by the liquefaction strength.

Acknowledgements

The authors would like to express their appreciation to the National Research Institute for Earth Science and Disaster Prevention for allowing the use of their K-NET record in this paper. This work was supported by JSPS KAKENHI Grant Numbers JP15K18111.

References

[1] Yasuda S, Harada K, Ishikawa K and Kanemura Y (2012): Characteristics of the liquefaction in Tokyo bay area by the 2011 off the Pacific Coast of Tohoku Earthquake. *Soils & Foundations*, **52** (2), 793-810.

[2] Tsukamoto Y, Kawabe S and Kokusho T (2012): Soil liquefaction observed at the lower stream of Tonegawa River during the 2011 off the Pacific Coast of Tohoku Earthquake. *Soils & Foundations*, **52** (2), 987-999.

[3] Sasaki Y, Towhata I, Miyamoto K, Shirato M, Narita A and Sako S (2012): Reconnaissance report on damage in and around river levees caused by the 2011 off the Pacific Coast of Tohoku Earthquake. *Soils & Foundations*, **52** (2), 1016-1032.

[4] Nagao Y, Sato T, Matsumaru T and Kiguchi, M: Shaking table test of model ground with spatial distribution of liquefaction strength, *Proceedings of the 49th Japanese National Conference on Geotechnical Engineering*, 1137-1138. (in Japanese)

[5] Nakazawa, H., Sugano, T. and Murakami, H. (2010): Case study on estimation of damage to runway pavement ground induced by liquefaction by geophysical exploration. *Journal of Japan Association for Earthquake Engineering*, **11**(6), 504-518. (in Japanese)

[6] Nakai K, Asaoka A, Sawada Y (2016): Extensive liquefaction damage in Urayasu city enhanced by surface wave induced around its irregularly-shaped boundary, *Japanese Geotechnical Society Special Publication*, **2**(19), 723-728.

[7] Miyata M, Iai S and Ichi K (1998): Estimation of differential settlements due to liquefaction. *Technical Note of the Port and Harbour Research Institute Ministry of Transport Japan*, 908. (in Japansese)

[8] Sato T, Hoshi T, Shinozaki Y, Kawakami T, Kudo A, Matsumaru T and Hasegawa H (2014): Liquefaction of the embankment constructed coal ash in the railway and the consequence assessment, *Proceedings of the 69th Annual Conference of the Japan Society of Civil Engineers*, 765–766. (in Japanese).

[9] Kudo A, Kurotsu A, Hasegawa H, Kiguchi M, Matsumaru T, Hoshi T and Takano, Y (2013): Liquefaction resistance characteristic of railway embankment material containing coal ash, *Proceedings of the 68th Annual Conference of the Japan Society of Civil Engineers*, 663–664. (in Japanese).

[10] Yoshimoto N, Orense R, Hyodo M and Nakata Y (2013). "Dynamic behavior of granulated coal ash during earthquakes. *Journal of Geotechnical and Geoenvironmental Engineering*, **140**(2).

[11] Uzuoka R and Borja RI (2012): Dynamics of unsaturated poroelastic solids at finite strain. *International Journal for Numerical and Analytical Methods in Geomechanics*, **36,** 1535-1573.

[12] Matsumaru T and Uzuoka R (2014): Dynamic analysis of embankment based on three phase porous media theory using elasto-plastic constitutive mode for unsaturated soil, *Journal of Civil Engineering (C)*, **70**(4), 395-411. (in Japanese)

[13] Oka F, Yashima A, Tateishi A, Taguchi Y and Yamashita S (1999): A cyclic elasto-plastic constitutive model for sand considering a plastic-strain dependence of the shear modulus. *Geotechnique*, **49**(5), 661-680.

[14] Armstrong PJ and Frederick CO (1966): A mathematical representation of the multiaxial Bauschinger effect. *C.E.G.B. Report RD/B/N731*.

[15] Tokimatsu K and Uchida A (1990): Correlation between liquefaction resistance and shear wave velocity. *Soils and Foundations*, **30**(2), 33–42.